RESEARCH: Original Research

Operando X-ray diffraction during laser 3D printing

Samy Hocine [1,2], Helena Van Swygenhoven [1,2,*], Steven Van Petegem [1], Cynthia Sin Ting Chang [1], Tuerdi Maimaitiyili [1], Gemma Tinti [3], Dario Ferreira Sanchez [4], Daniel Grolimund [4], Nicola Casati [5]

[1] Photons for Engineering and Manufacturing, Paul Scherrer Institut, Forschungsstrasse 111, 5232 Villigen PSI, Switzerland
[2] Neutrons and X-rays for Mechanics of Materials, IMX, École Polytechnique Fédérale de Lausanne, Route Cantonale, 1015 Lausanne, Switzerland
[3] SLS Detectors Group, Paul Scherrer Institut, Forschungsstrasse 111, 5232 Villigen PSI, Switzerland
[4] MicroXAS Beamline, Paul Scherrer Institut, Forschungsstrasse 111, 5232 Villigen PSI, Switzerland
[5] Materials Science Beamline, Paul Scherrer Institut, Forschungsstrasse 111, 5232 Villigen PSI, Switzerland

Laser based additive manufacturing allows to build a designed shape layer-by-layer, offering versatility and flexibility to many metallurgical sectors. The fast cooling rates and repeated heat cycles depending on the laser and scanning parameters are not easily measurable with conventional methods. Thus, advanced predictive computational simulations, required to reduce trial and error lead time, are difficult to validate.

A newly developed in operando X-ray diffraction device implemented at a synchrotron beamline, taking advantage of the high brilliance and the fast detectors available, brings the missing link with numerical methods. By performing *operando* experiments on Ti-6Al-4V with different printing parameters, the temporal evolution of the low and high temperature phases are followed, the heating and cooling rates are measured for the powder and the solid material; and the formation of residual stresses in the β phase is demonstrated. Moreover it is shown that the parameter that has the largest influence on the evolving microstructure is the scanning strategy, introducing a size effect related to the scanning length.

Introduction

Selective laser melting (SLM) is an additive manufacturing (AM) technique that uses a high power-density laser to selectively melt and fuse metallic powders together, under an inert atmosphere in order to build layer-by-layer 3D structures. AM techniques are believed to be very promising to make complex geometries and open structures with thin walls and hidden open volumes or channels. It is well known that fully dense material can be produced when using optimal deposition parameters. However, the obtained microstructures and properties depend strongly on the laser and scanning parameters, scanning strategies, powder characteristics and powder bed temperature [1–6]. Consequently, trial-and-error methods to determine the optimal SLM processing parameters are tedious.

Numerical modelling approaches could help predicting and understanding the role of individual parameters, but because of the multiple length and time scale character of the physical process involved [7,8], the models become rapidly very complex. Therefore, multi-physics numerical approaches that can address the powder scale [9–14] and/or the material deposition scale with FEM-based methods [15–22] are emerging. Computational models need to be validated, which requires tailored experiments or,

* Corresponding author at: Paul Scherrer Institut, Forschungsstrasse 111, CH-5232 Villigen PSI, Switzerland.
E-mail address: Van Swygenhoven, H. (helena.vs@psi.ch)

https://doi.org/10.1016/j.mattod.2019.10.001

ideally, real-time measurement techniques that provide temperature profiles and cooling rates [23–26].

With the recent developments of ultra-fast detectors and the high flux provided by third generation synchrotron radiation sources, it is now possible to perform experiments with a time-scale resolution relevant for laser-based AM. Fast X-ray diffraction methods have revealed precipitation kinetics during high cooling rates in Al-based alloys and followed phase transformations in a Ti-based alloy [27,28]. Fast X-ray imaging allowed to capture the melt pool and powder dynamics during laser interaction with powder confined between two X-ray transparent plates [29–31]. The experiments provided information on the shape of the melt pool and on the development of pores during laser scanning. The laser-powder interaction during the SLM process is however a full 3 dimensional problem. Looking at the rapid melting and solidification of one powder granule, or looking at the laser interaction with powder that is confined between two plates, does not capture the full complexity of the layer-by-layer deposition process. It is with this idea in mind that we have developed a miniaturized SLM device (MiniSLM) to build 3D structures from CAD files during X-ray diffraction. The evolution of a probed volume throughout layer-by-layer deposition under an argon flow can be followed, and the influence of laser and scanning parameters investigated.

The material investigated is Ti-6Al-4V (wt.%), an alloy that is used in many additive manufacturing studies because of its high specific strength, low mass density and high corrosion resistance [3,32]. Its biocompatibility has also motivated researchers to explore the compressive properties of open lattice structures that can be easily made by AM methods [3,33,34], as well as the influence of the part orientation relative to the build direction [35]. Ti-6Al-4V powder experiences a phase transformation $\alpha/\alpha' \rightarrow \beta \rightarrow$ liquid during laser melting. The fast scanning speed, characteristic of the AM processes, induces high thermal gradients and when temperature drops below the β transus, the material transforms into an α/α' microstructure strongly dependent on the cooling rates [1].

Typically, a fine acicular α' martensite with a high density of defects such as twin boundaries, dislocations and stacking faults is formed within columnar prior β-grains [1–3]. Since the prior β-grains grow epitaxially with a [0 0 1] crystallographic orientation along the build direction due to directional cooling, a strong crystallographic texture is formed [36,37]. Such microstructures have poor ductility, fracture toughness and fatigue behaviour [5], therefore a lot of research is devoted to adjust the microstructure by post-heat treatments and hot isostatic pressing to decompose the martensite into an $\alpha + \beta$ microstructure.

The $\alpha + \beta$ microstructure reached after post treatments depends however on the original microstructure developed during SLM. This highlights the importance of understanding the microstructure development as function of the processing parameters. It has been shown that the volume energy density in the SLM process influences not only the acicular α' microstructure, but also the partitioning of the V, a β stabilizer, which conditions the remaining nanometre β films after cooling. Residual β films and lattice defect arrangements are precursors of the evolving β phase during post-treatments, and their distribution will determine the final $\alpha + \beta$ microstructure [37,38].

Changing the energy density while keeping porosity low, is usually done by changing simultaneously the laser power, scanning velocity and hatch distance, without detailed knowledge of each individual parameter on the evolution of the melt pool [39]. Very little attention has been paid to the scanning strategy i.e. the length of the scanning vector. The latter can be varied by using chessboard or island scanning patterns instead of simple bidirectional line scans. The length of the line scan is however important when either making complex shapes, structures with open channels or open lattice structures [40,41].

Here we present *operando* diffraction experiments during printing of a Ti-6Al-4V commercial alloy using our newly developed MiniSLM. We reveal the influence of the laser and scanning parameters on the temperatures reached during the process, the cooling rates and the duration the β phase exists. By performing experiments with different scanning strategies, we demonstrate that printing short scanning lines results in a coarsening of the prior β grains, lowers the cooling rates after solidification, and therefore forms a substantial different microstructure.

Results

Operando SLM device

We have designed and built a miniaturized SLM setup, equipped with the basic functionalities of commercially available SLM machines, and further optimized for installation at synchrotron beam lines. Fig. 1a and b display the main components. A collimated infrared laser beam (1) is deflected by a 2-axis scanning unit (2) into the main chamber (3). Details on the laser unit can be found in the Methods section. The laser beam is focused onto a 12×12 mm^2 build stage (4) that can be translated vertically with a travel range of 12 mm and sub-micron step size. The build stage can be heated up to 180 °C using a silicon–nitride resistive heater mounted inside a custom-made zirconia ceramic element (5). The temperature is monitored by a fine gage unsheathed thermocouple and controlled by a conventional PID algorithm. Powder recoating is based on a hopper feeding system. The powder reservoir (6) can be moved across the baseplate with the aid of a motor-spindle assembly (7).

The device is completely closed, preventing laser light or particles to escape. The chamber is continuously flushed with high purity argon gas. With the aid of manual flow meters, a slight overpressure is created in the chamber to avoid oxygen contamination by the outside atmosphere. The oxygen level is monitored after the outlet of the chamber with an 0.2% accuracy. Different sets of filters are placed along the inert gas circuit to sieve the particles generated during the printing. In the chamber, after the input and before the output, stainless steel filters (8) with a 1 μm opening are used to avoid large particles escaping the machine. For sub-micron particles, a PTFE filter with an 0.2 μm opening is placed after the outlet but before the oxygen sensor. Finally, a water-based filter is placed after the pump to trap any residual small particles. The whole setup (laser, scanning unit and printing chamber) is cooled down with a closed-loop air–water exchange based chiller.

The printing chamber exhibits two glassy carbon windows (9) with thicknesses of 100 μm and 500 μm for the incoming and outgoing X-ray beam, respectively. Glassy carbon has the advan-

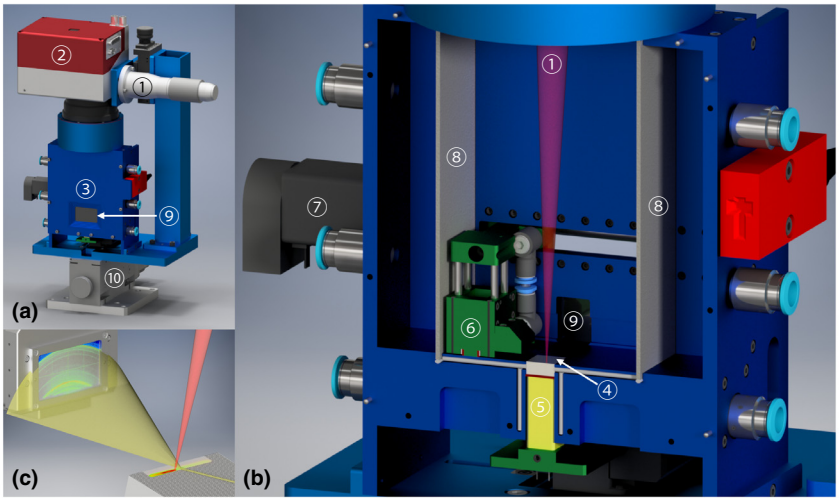

FIGURE 1

Rendered 3D model of the *operando* MiniSLM device: front view (a), zoom in open build chamber (b) and scattering geometry (c). A detailed explanation of the different components (as indicated by the numbers 1–10) is given in the text.

tage to be opaque to visible and infrared light, whereas it is virtually transparent for high-energy X-rays. The size of the exit window was chosen such that diffraction angles of more than 70° can be obtained.

The machine is mounted on a heavy load tilting stage that allows rotating the complete setup ±20° around a horizontal axis (10). This allows the incoming beam to interact with the powder on the build stage.

Video S1 shows the various steps of a typical *operando* SLM experiment. First, the build stage is lowered by an amount corresponding to the chosen layer thickness. Then, a thin layer of powder is spread over the build plate by the powder feed system. A hardware trigger starts both the laser operation and the acquisition of X-ray diffraction spectra by the fast detector. The laser scanning head deflects the laser on the build stage and locally melts the powder to form solid material. This process can be repeated multiple times to form a 3D structure embedded in the powder. The *operando* experiments described in this work have been performed at the MicroXAS beam line (Fig. 2), located at the Swiss Light Source. Details on the setup can be found in the Methods section. The scattering geometry is schematically presented in Fig. 1c. Cuboidal-shaped samples with various sizes are printed near the edge of a Ti-6Al-4V build plate. The experiments reported in this work are performed in reflection geometry. Here, the MiniSLM machine is tilted by 15 degrees and the X-ray beam is positioned at ~1 mm from the outer edge. A fast EIGER detector intercepts the diffracted beam at a distance of 80 mm and records diffraction patterns at a frame frequency of 20 kHz.

Operando X-ray diffraction

We investigate the evolution of the diffraction patterns during printing of rectangular layers, each consisting of 33 lines with 8 mm length, a hatch distance of 60 μm and layer thickness of 30 μm. The laser was operated at 250 W with a scanning speed of 600 mm/s. This set of parameters was chosen based on a parametric study to minimize pore formation. The reference sample for this work had a density of 99.8% determined by optical microscopy imaging. During printing, 16,000 diffraction patterns were recorded with a time resolution of 50 μs. The X-ray beam had a size of $80 \times 140\ \mu m^2$ (full-width at half-maximum – FWHM). Fig. 3a displays the diffraction intensity as a function of time and diffraction angle for the 3rd layer. The results for the other layers provide a similar image. The angular range includes the (0 0 2), (0 1 1), (0 1 2) and (1 1 0) reflections of the α/α′ phase and the (0 1 1) and (0 0 2) reflections of the β phase. Fig. 3b displays the individual diffraction patterns prior to printing and after $t = 276$ ms. Prior to printing, no β phase can be detected in the freshly deposited powder. The laser starts scanning at $t = 130$ ms, as indicated by the white arrow in Fig. 3a. With a scanning speed of 600 mm/s, the laser takes 13.3 ms to print a single line. During printing of the first 9 lines, the temperature in the volume probed by the X-ray beam slowly increases, evidenced by a slight angular shift of the diffraction peaks. When

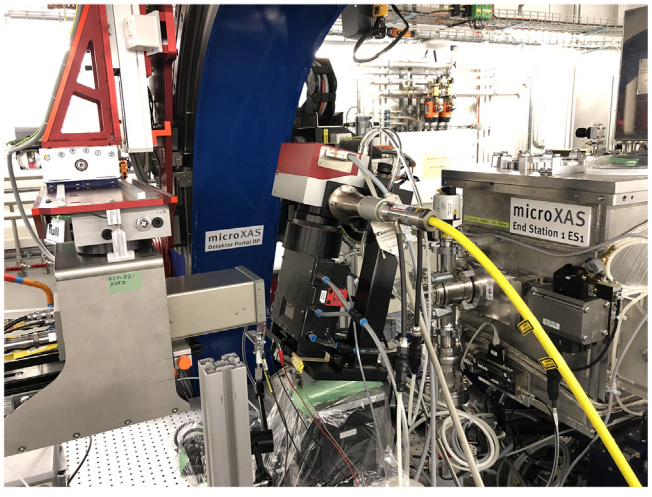

FIGURE 2

Picture of the MiniSLM mounted at the MicroXAS beamline.

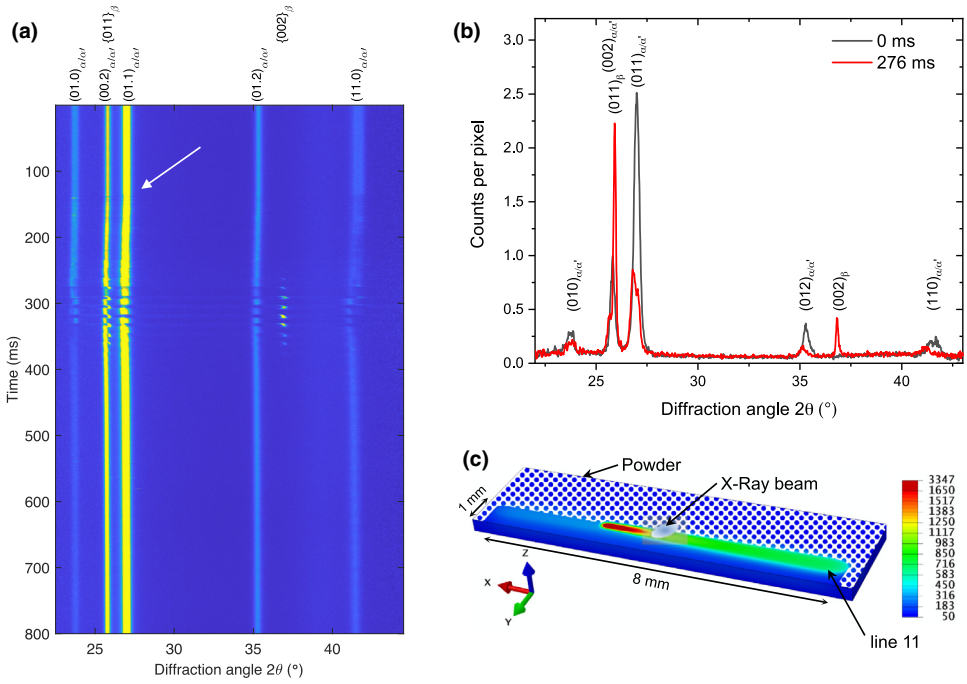

FIGURE 3

(a) Phase evolution during printing of a single layer, shown as an intensity vs. diffraction angle and time by stacking 16,000 individual diffraction patterns. The white arrow indicates the start of the printing process, (b) diffraction patterns recorded prior to printing and during printing of the 11th line at t = 276 ms, (c) schematic representation of the relative position of laser, X-ray beam and HAZ at t = 276 ms. (Temperature scale in degree Celsius).

the laser beam approaches the position of the X-ray beam, the angular shifts become more pronounced, the intensities of the α/α′ peaks start fluctuating and the β phase appears. Fig. 3c shows a snapshot at t = 276 ms, generated by FEM simulations, which corresponds to the moment the laser is printing the 11th line. After printing only the martensitic α′ phase is present, as shown in Fig. S3 in the Supplementary Data. This is expected as it is known that for cooling rates above ~400 °C/s the β phase exhibits a martensitic transformation to the α′ phase, where during SLM cooling rates are of the order of 10^4–10^6 °C/s [42].

Fig. 4a and b show respectively the integrated intensity of the (0 0 2)β reflection and the (0 1 1)α reflection as a function of time. At the moment the laser is switched on (t = 130 ms) the intensity of the α peak starts fluctuating strongly, which can be ascribed to moving powder and the presence of a plasma plume [43]. The β phase can be detected while printing lines 10–18. The gradual increase and decrease of the β phase with each line, and corresponding decrease in α phase can be understood considering the overlap between the melt pool with its surrounding heat affected zone (HAZ) and probed X-ray volume, as is illustrated in Fig. 4d. Here, we consider as HAZ the region where the temperature rises above the β transus. We define the total area probed by the X-ray beam (V_{XR}) as twice the full-width at half-maximum of the X-ray beam profile. In cycle 10, the centre of the laser beam is approximately 240 μm away from the centre of V_{XR}, which is well beyond the expected size of the melt pool. Nevertheless, the heat flow in the powder is high enough to partially induce the α to β transition in the probed powder volume. During cycle 14, the laser and X-ray beam experience the largest overlap. Here, the highest intensity of β is measured while the α diffraction peaks vanish completely.

Between 270 ms and 350 ms, the intensity of the α phase decreases rapidly each time the laser passes V_{XR}. Simultaneously, the intensity of the diffuse scattering increases rapidly (see Fig. 6). This allows a very precise determination of the time needed for the laser to print multiple lines and the settling time the laser needs between two consecutive lines. For the setup used in this work the scanning head has a settling time of 0.63 ± 0.05 ms, which was found to be independent of scanning speed or dimensions of the printed structure.

Thermal expansion and contraction changes the lattice spacing between crystallographic planes during heating and cooling, and thus the position of α and β diffraction peaks. But also internal stresses and changes in chemical composition can change lattice spacing. In a first approximation we assume that during initial cooling from the melt, the decrease in lattice spacing of the β phase is solely due to thermal contraction. The temperature evolution is then calculated from the lattice spacing using thermal expansion coefficients tabulated in [44], the results are shown in Fig. 4c. Upon further cooling the lattice spacing of the β phase suddenly increases, which coincides with the β -> α transition. This is indicated by the green curve in Fig. 4c. In this regime it is not possible to reliably deconvolute the contribution of thermal, chemical and stress effects and therefore no cooling rates can be reported.

As shown in Fig. 4c, the average temperature of the α phase in V_{XR} increases very shortly after the laser is switched on. The fluctuations correspond with the laser approaching and traveling away from V_{XR}. These fluctuations are not only visible during the cycles where transformation to β is observed, but also earlier and later on. During the three sequential scanning lines after the laser passed V_{XR}, the average temperature of the α phase reaches

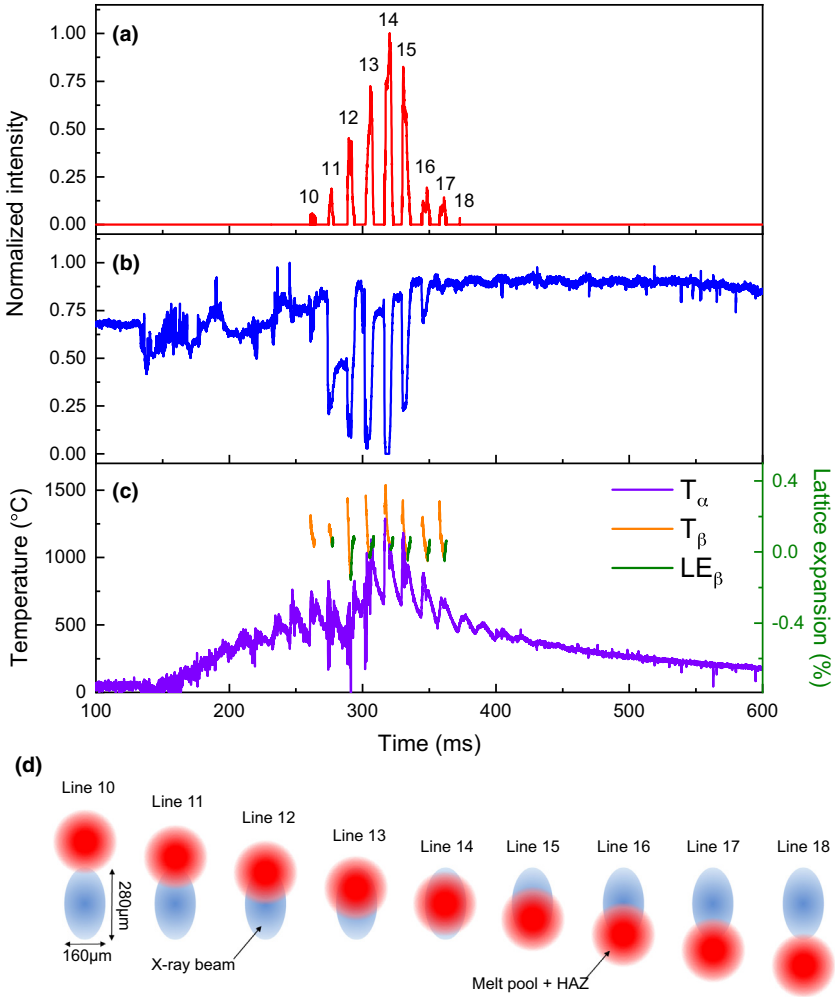

FIGURE 4

Evolution of the integrated intensity of the $(0\,0\,2)_\beta$ reflection (a) and the $(0\,1\,1)_\alpha$ reflection (b) as a function of time during printing of a 8 × 2 mm^2 layer, (c) the equivalent temperature evolution, (d) schematic representation of the relative position of the laser line scan (red) and X-ray beam (blue) when the laser is at the same X position as the X-ray beam (see Fig. 3c).

respectively 1100 °C, 870 °C and 700 °C. During these cycles, V_{XR} still partially transforms to β, reaching temperatures above 1200 °C, reflecting the strong temperature gradient in V_{XR}.

In line 14 to 15, the average temperature of β decreases rapidly from 1500 °C to a temperature well below the β transus (1000 °C). The α phase is however already visible at temperatures above the β transus e.g. resp. 1300 °C and 1200 °C. In cycles 16 and 17, the α phase appears only at temperatures well below the β transus. These differences in average temperature are due to the fact that in lines 16 and 17 the β phase is only formed in the outer region of V_{XR} closer to the centre of the laser spot. This is graphically explained in Fig. 4d. It is well known that the thermal cycles after the laser crossed V_{XR} influence the final α lath microstructure [1,45].

Fig. 5a highlights the evolution of the integrated intensities, temperature and lattice expansion of both phases during cycle 14. The same colour scheme as in Fig. 4 was employed. Fig. 5b–d shows three snapshots of the relative position of the melt pool, HAZ and X-ray beam, obtained from FEM simulations. Just before the laser approaches $V_{XR,}$ only the α/α′ phases are present with an average temperature of 750 °C. At $t = 315.8$ ms the intensity of α peaks drop sharply and the first signs of β are seen at $t = 316.2$ ms. This transition is followed by a raise in the average temperature of α and β. At $t = 317.5$ ms, the average temperature of β has reached 1600 °C, which is close to the theoretical melting temperature of Ti-6Al-4V. The intensity of the β phase increases rapidly during 0.8 ms, a time interval during which the laser travels 0.5 mm. The relative position between laser and V_{XR} is shown in the Fig. 5c. In other words, the laser has passed well beyond V_{XR} before the maximum is reached, confirming the slower kinetics of the phase transformation and the superheating above the β transus temperature [46]. During the next 3.5 ms, the average temperature of β decreases fast, with an initial cooling rate of $-3.6 \pm 0.6 \times 10^5$ °C/s. When the β transus is reached, the β intensity starts dropping and the α phase reappears. A tensile residual stress is formed in the $(0\,0\,2)_\beta$ planes, as reflected by the green curve. During 9 ms, α cools down reaching an average temperature of 650 °C. During this time, the laser has travelled 5.4 mm and has approached V_{XR} again (schematically presented in the Fig. 5d). The total duration that V_{XR} is fully in the β phase while printing this line amounts to 2 ms.

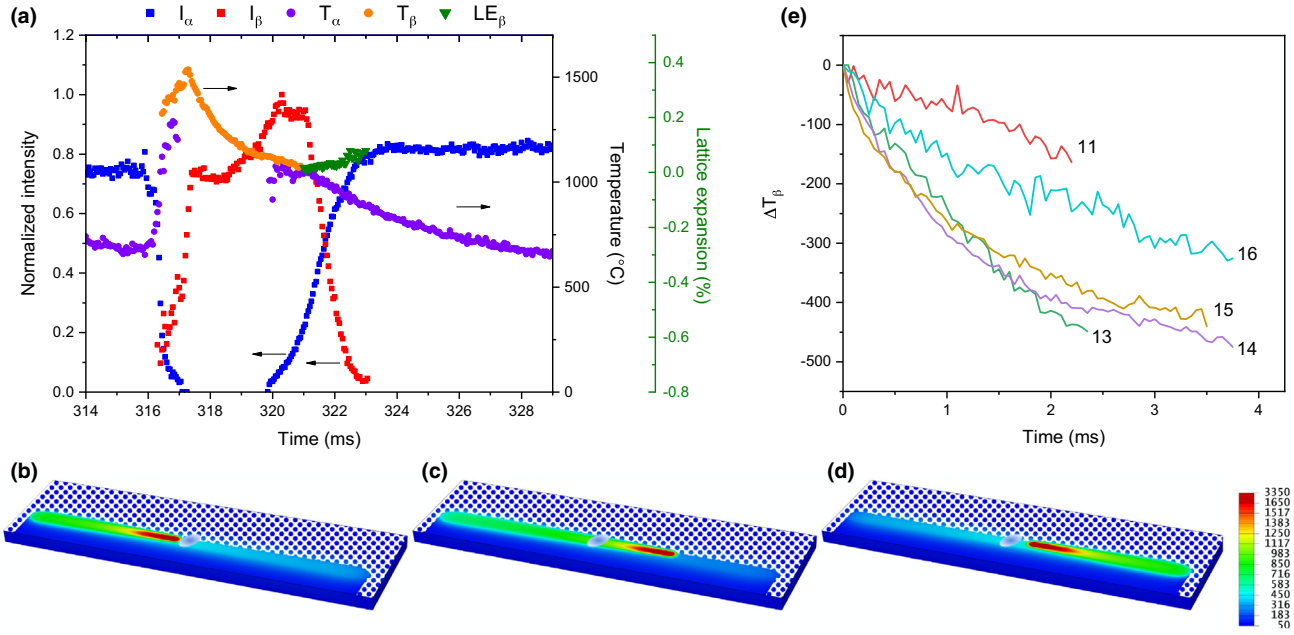

FIGURE 5

X-ray diffraction results during printing of a single line. (a) Evolution of integrated intensity, temperature and lattice expansion in the α and β phase during printing of line 14, (b)–(d) schematic representation of the relative position of the X-ray beam compared to the melt pool and HAZ (temperature scale in degree Celsius), (e) temperature evolution (ΔT_β) in the β phase for selected cycles. The curves are shown up to the point where the α phase is formed.

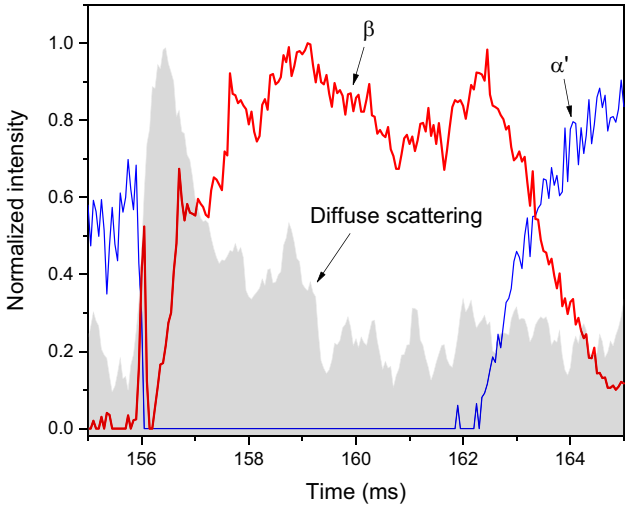

FIGURE 6

Evolution of the α/α′ and β phase during a single passage of the laser beam probed by a 30 × 35 μm^2 X-ray beam. The intensity of the diffuse scattering between the diffraction spots is shown in grey.

Fig. 5e displays the evolution of the temperature the β phase for the various cycles. During cycle 11 the X-ray beam only probes the powder, which is known to have a lower heat conductivity compared to the solid [47]. This results in a relatively low cooling rate. In cycles 13–15 the laser passes directly through V_{XR}, resulting in higher averaged temperature and cooling rates. In cycle 16 the laser beam has passed V_{XR} but cooling rates are high compared to cycle 11 because V_{XR} is now solidified.

A second series of experiments was performed with an X-ray beam with a size of 30 × 35 μm^2 (V_{XR} = 60 × 70 μm^2), which is smaller than the expected size of the melt pool. The scan speed was 400 mm/s. This allows observing the transition α → β → liquid during heating. Fig. 6 displays the evolution of integrated intensities of the $(0\,1\,1)_\alpha$ and $(0\,0\,2)_\beta$ diffraction peaks during one cycle. In grey the evolution of the diffuse scattering is shown. At the moment the laser beam arrives at V_{XR} the intensity of diffuse scattering strongly increases, which is due to a combination of thermal diffuse scattering and scattering from the melt pool. The rise time of the diffuse scattering is 0.7 ms, which corresponds to the time needed for the laser beam to pass V_{XR}. Simultaneously, the intensity of the α phase decreases very fast and a short (0.2 ms) β signal is visible. Upon further heating no diffraction peaks are visible, indicative for a complete melting of V_{XR}. During cooling the intensity of the diffuse scattering decreases and the β peak reappears.

Influence of the laser parameters

Fig. 7 highlights the influence of the laser power on the phase evolution during printing. All experiments are performed with a scanning speed of 600 mm/s and a hatch distance of 60 μm. The laser power was varied from 175 W to 250 W. Fig. 7a shows that both the number of cycles where β is created and the period during which β is visible is longer with increasing power. This is expected, as with higher laser power the size of the melt pool and HAZ expands. Fig. 7b compares the maximum cooling rates while printing the line with maximum overlap between the laser and X-ray beam as a function of power. The cooling rates are determined by the tangent of the temperature versus time curves. With increasing power the cooling rate in the β phase decreases, while it increases in the alpha phase. This can be understood, considering that that lower power results in a smaller melt pool and consequently higher thermal gradients within V_{XR}.

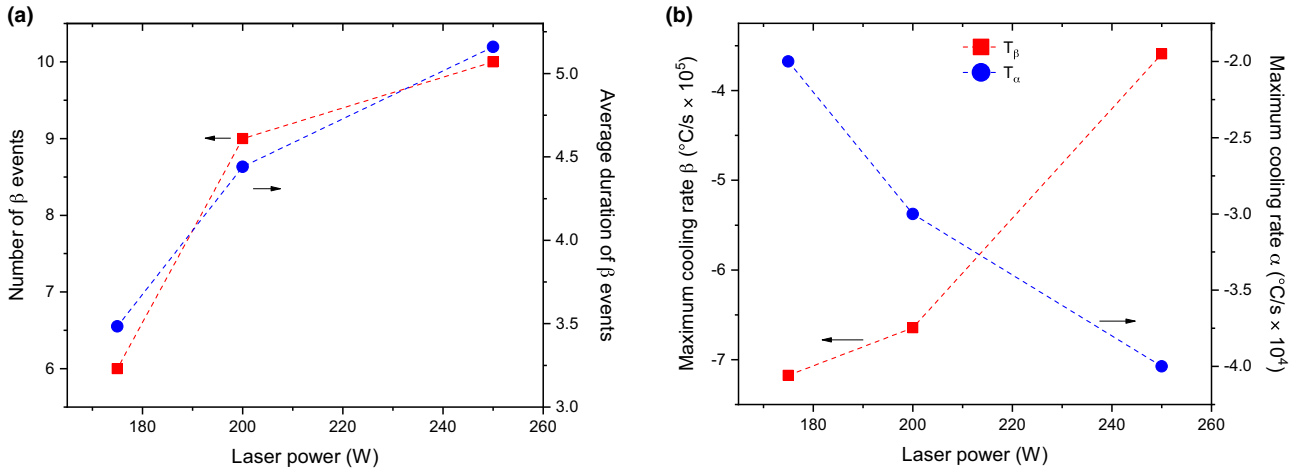

FIGURE 7

Influence of laser power on the microstructure evolution during printing. (a) Number and average duration of β events, (b) maximum cooling rates in the α and β phase as a function of laser power.

Influence of scanning strategy

The above experiments demonstrate the evolution of the phases during the scanning of an 8 mm line, which is long enough to allow β be fully transformed back into α before the laser hits back the probed volume V_{XR}. In this section we investigate what happens when the length of the line scan is decreased to dimensions used during scanning strategies such as chessboard or island scanning.

Fig. 8a–c show the evolution of the intensities of the $(0\,0\,2)_\beta$ and the $(0\,1\,2)_\alpha$ reflection during a time interval of 200 ms while printing squares with sizes of $2 \times 2\,mm^2$, $4 \times 4\,mm^2$ and $6 \times 6\,mm^2$. The laser was operated at 250 W, with a scanning speed of 600 mm/s and a hatch distance of 60 μm. The results for the 6x6 mm square is similar to those obtained for the sample with 8 mm scan vector length (Fig. 2a); in each cycle β is transformed back to the α phase during cool down. This is however not the case for the smaller samples. Here, once the laser crosses V_{XR} and the volume is fully transformed into β, V_{XR} remains fully in the β phase during subsequent cycles. The time needed for the laser to come to the same point in the centre of the samples is 4 ms and 7.3 ms for the $2 \times 2\,mm^2$ and $4 \times 4\,mm^2$ squares, respectively. As a consequence, the temperature remains sufficiently high to prevent the transformation back to α before the laser returns. V_{XR} remains in the β phase during 70 ms (17 cycles) in the $2 \times 2\,mm^2$ square and 45 ms (7 cycles) in the $4 \times 4\,mm^2$ square.

Fig. 9 shows for the $2 \times 2\,mm^2$ sample the intensity evolutions (a), the average temperature in V_{XR} (b) as well as the lattice expansion reflecting the building up of residual stress. Fig. 9c–e provide a schematic representation of the relative position of X-ray beam and the melt pool with HAZ for the three points indicated in Fig. 9a. Between scan line 8 and 12, α and β co-exist, the average temperature in the α phase raises up to about 800 °C and strong temperature fluctuations are be observed for β between 1600 °C and the β transus, with maximum heating and cooling rates of 2×10^6 °C/s and -3×10^5 °C/s, respectively.

At line 13, V_{XR} contains no α phase anymore and the intensity of β increases steadily. While more and more β phase is formed, the average temperature decreases. Simultaneously the cooling rate decreases down to -1.5×10^4 °C/s. Similar to the case of the larger samples, when α starts forming, the lattice expansion of β reflection suggests the presence of residual stress in β (shown by green curve in Fig. 9b).

It is no surprise that this different temperature history changes the resulting α microstructure. Fig. 8d–f show EBSD pictures of the second last layer. The microstructures of this layer consist of blocks (outlined by dashed lines) that have the same size as the prior β grains, shown in Fig. 8g–i. Such a block pattern was also observed [1] and [48]. However, the size of the blocks was related to the hatch spacing while in our case, the size of a block is related to the duration and size of material staying above the β transus, which is largest in the 2x2 mm^2 sample. High resolution EBSD shown in Fig. 8j-i, shows a hierarchical α′ martensitic structure formed in a basket weave pattern. At least 4 size variations of α′ can be seen. The primary α′ needles have a width of 2–3 μm while for the last generation it can be as thin as 50 nm. The average width of the α′ needles decreases as the print cross-section increases.

The textures of the second last layer printed of all samples are relatively weak (maximum intensity of pole fig. ≈5), Fig. 8d–f. This is also shown by the inverse pole figures in S5 in the Supplementary Data. The weak textures are attributed to the high number of α′ variants within each β grain [49] calculated from the α′ orientation. The texture of the prior β grains seems to be weak with most of the grains having large misorientation relationship to the neighbouring grains.

Discussion and conclusions

The MiniSLM device in combination with high-flux synchrotron X-ray diffraction and an ultra-fast low noise detector allows following the microstructural evolution during 3D laser printing with high time resolution. For the case of Ti-6Al-4V we are able to track the evolution of the low and high temperature phases, heating and cooling rates, the formation of residual stresses in

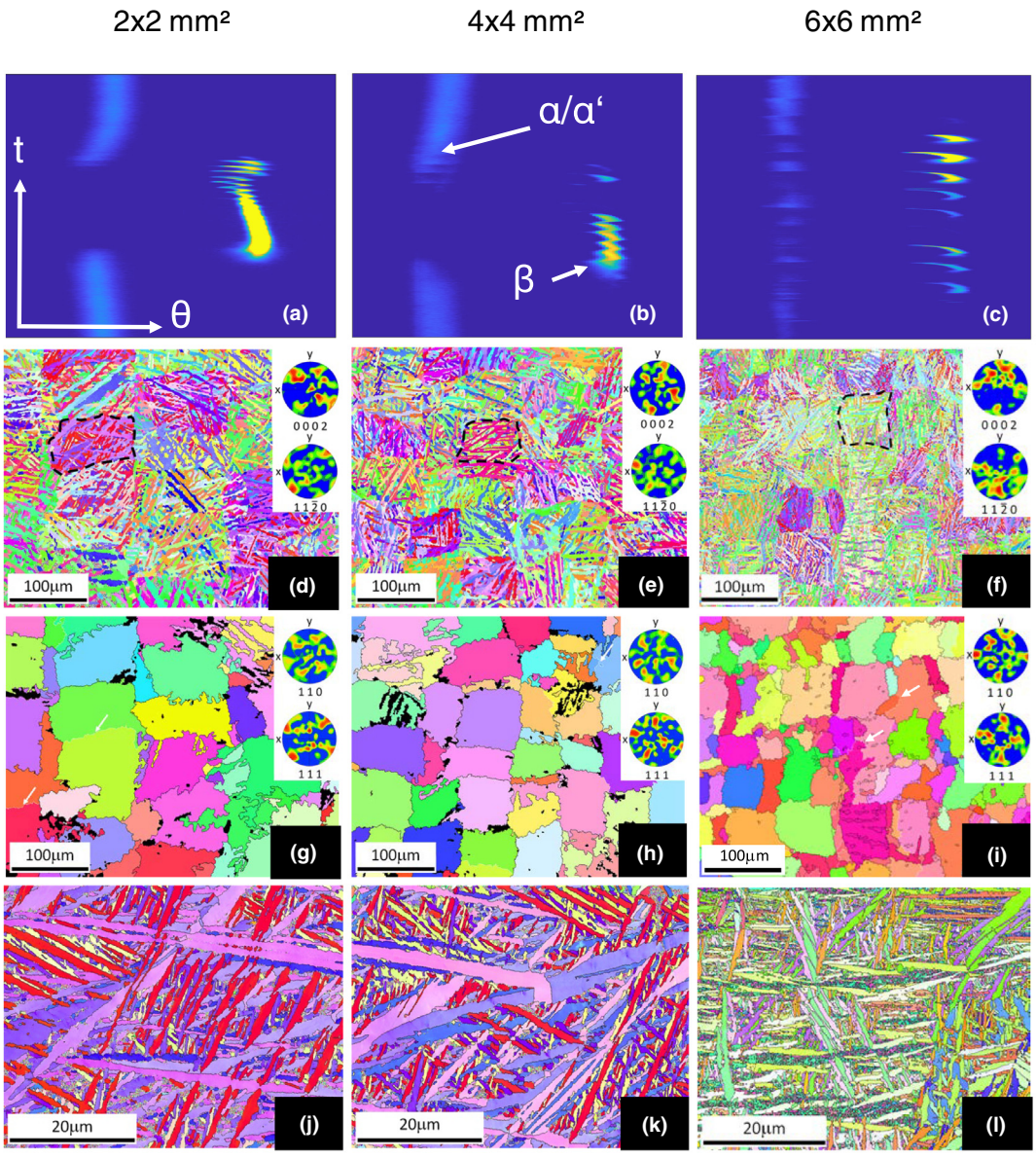

FIGURE 8

Influence of scanning strategy on resulting microstructure. Evolution of the intensities of the $(0\ 0\ 2)_\beta$ and the $(0\ 1\ 2)_\alpha$ reflections while printing squares with sizes of (a) 2×2 mm^2, (b) 4×4 mm^2 and (c) 6×6 mm^2. IPF maps of the building planes of (d) 2×2 mm^2 (e) 4×4 mm^2 and (f) 6×6 mm^2 samples, with insets showing the {0 0 0 2} and {11–20} pole figures. IPF maps of the reconstructed prior β grains for (g) 2×2 mm^2, (h) 4×4 mm^2 and (i) 6×6 mm^2 samples with their {1 1 0} and {1 1 1} pole figures. The colour schemes of the IPF maps and the IPF representing the textures of the area in the maps are shown in Fig. S4 in Supplementary Data. White lines are low angle grain boundaries with misorientation angles between 5° and 15° and black lines are high angle grain boundaries. The arrows point to some of the low angle boundaries. High-resolution IPF maps showing basket weave microstructures with variants of α′ martensitic in (j) 2×2 mm^2 and (k) 4×4 mm^2. In (l) 6×6 mm^2, α′ laths with smaller aspect ratio are found.

the β phase and the difference in heat dissipation between powder and the solid.

Apart from the processing parameters such as laser power, hatch distance and scanning speed; the scanning strategy plays an important role in the final microstructure after printing. Numerous scanning strategies exist, such as raster, helix, island or inter-layer stagger scanning. Often the length of the scanning vectors is reduced in order to lower residual stresses, although some contradictory results exist in literature regarding its effect [50,51]. Here, we have shown that the length of the scanning vector significantly influences the thermal history at a given point in the printed structure. This is crucial for materials that experience phase transformations during solidification. For the case of Ti-6Al-4V, we have shown that by reducing the length of the scanning vector the high temperature β-phase exists over a longer time and exhibits lower cooling rates. This results in larger prior-β grain sizes, and different texture and morphology of α′ martensite. This is particularly important when printing parts with hollow channels or open lattice structures. Here, the use of varying scan vector lengths is unavoidable, which may lead to components with spatially heterogeneous mechanical properties.

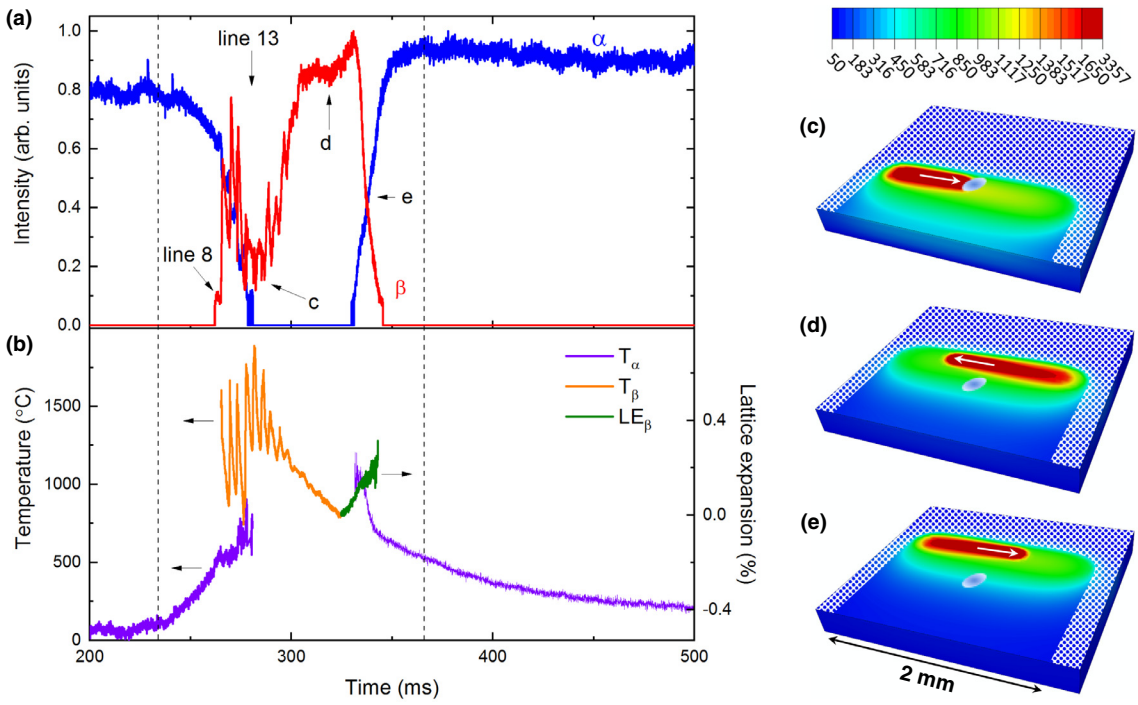

FIGURE 9

Diffraction results for the 2 × 2 mm^2 sample. (a) Evolution of the integrated intensities of the $(0\,0\,2)_\beta$ and $(0\,1\,1)_\alpha$ diffraction peaks, (b) corresponding temperature and lattice expansion (LE). The dashed lines indicate the start and end of the print process. (c)–(e) Schematic representations of the relative position of the X-ray beam and melt pool/HAZ, the white arrow indicates the scanning direction (temperature scale in degree Celsius).

The time resolved measurements obtained from *operando* diffraction provide information averaged over the volume probed by the X-ray beam, and can be used for validation of the many FEM-based models addressing the material deposit scale [16,20,52]. Scaling the X-ray beam profile to the mesh size or vice versa, will optimize the synergetic aspect. Experiments can be tuned to validate some aspects of simulations, as for instance the differences in cooling rate between solid and powder [16]. *Operando* experiments can contribute to the understanding of the influence of micro-alloying in aluminium alloys on the evolving microstructure [53,54]. Furthermore, such an experiment allows to determine the laser settling time, i.e. the time the laser is turned off and the melt pool cools down significantly before a new line is printed. This settling time is often overlooked when modelling the actual printing procedure, which leads to an overestimation of the size of the melt pool at the edges of the printed structures. This becomes particularly critical when modelling small structures.

The results discussed in this work are obtained by monochromatic X-ray diffraction in reflection mode with a moderate X-ray energy (12 keV). This provides information from the last deposited layer only. Alternatively, the *operando* measurements can also be performed in transmission mode when the X-ray beam is positioned sufficiently close to the edge of the build plate. Here the diffracted signal results as an average of the contribution of multiple layers. A further possibility is the use of energy-dispersive X-ray diffraction [55] which allows obtaining depth-sensitive information. Last but not least, an *Operando* experiment could be followed up by *in situ* heating to optimize post-annealing treatments for minimizing residual stress and optimizing the microstructure.

Methods

Material characterization

Ti-6Al-4V ELI (extra low interstitial, grade 23) gas atomized spherical powder was acquired from LPW Technology LTD. (Widnes, United Kingdom). The particle size distribution was measured by a laser diffraction particle size analyzer Partica LA-950 V2 system (Horiba, Tokyo, Japan). Fig. S1a in Supplementary Data shows that the powder size ranges between 5–60 μm with average size of 33 μm. To investigate the powder characteristics and chemical composition, a field emission gun scanning electron microscope (FEG SEM) Zeiss NVision-40 equipped with an energy dispersive X-ray spectrometer (EDS) analysis system from Oxford Instruments was used. Fig. S1b in Supplementary Data reveal the spherical nature of the powder and little porosity. The chemical composition of the powder is: Ti-6.35 wt%Al-3.46 wt%V-0.16 wt%Fe. Phase determination was performed by conventional X-ray diffraction measurements on a D8 ADVANCE (Bruker Corporation) with a Cu-Ka radiation source. Fig. S1c in Supplementary Data shows the diffraction pattern of the powder and corresponding Rietveld analysis by TOPAS [56] The powder consists of a mixture of hexagonal α (62 wt%) and α′ (38 wt%) Ti-phases. No cubic β-phase was observed.

The texture and grain size of the printed samples was investigated by Electron Backscatter Diffraction (EBSD) using a field emission gun scanning electron microscope (FEG SEM) Zeiss ULTRA 55 equipped an EDAX Hikari Camera operated at 25 kV

in high current mode with a 120 μm aperture. The samples were mechanical slightly polished using 3 μm diamond suspension and up to 0.04 μm colloidal silica to obtain a smooth surface for EBSD but not too deep as we wanted to observe the microstructures and textures for the last layer. Low and high-resolution mapping was performed with step sizes of 1 μm and 0.1 μm, respectively. The software package ARPGE [57] was used to reconstruct the β phase from the EBSD data. Post processing of the EBSD data and map reconstruction was done with the EDAX OIM Analysis 7.3 software package. IPF maps were cleaned up using grain dilation method to remove bad indexing points.

The density of a reference sample was determined from a cross section perpendicular to the build direction. The surface was polished and an image was taken with an optical microscope (Leica DMRX). The image was post processed with the software ImageJ into a black (pores) and white (metal) image. The ratio of the two was then calculated with the same software, resulting in a 99.8% density.

Laser scanning system

The laser source used this experiment is a 500 W redPOWER® continuous wave (CW) Fiber Laser (SPI Lasers Ltd, UK). It operates at a wavelength of 1070 ± 10 nm with a beam quality factor of $M^2 < 1.1$. The laser beam is directly collimated as a parallel Gaussian beam (ø9.6 mm at $1/e^2$) into a 2-axis deflection-scanning unit SuperScan III (Raylase GmbH, Germany) with 15 mm input aperture. Two fused silica mirror galvanometers with di-electric coating and a reflectivity of more than 99.5% at a wavelength of 1064 nm are piloting the beam in 2 dimensions. The beam is focused down to a ø100 μm spot size through a F-Theta lens (Sill Optics, Germany) with 163 mm focal length. The focused laser beam enters the printing chamber through a 500 μm thick fused quartz window (UQG Optics, UK) with on both sides an anti-reflection coating with a reflectivity smaller than 0.5%. The laser and scanning unit are piloted with a SP-ICE-3 board and the WeldMARK software (Raylase GmbH, Germany). Communication between the SP-ICE-3 board and LabVIEW is achieved over a standard ActiveX communication protocol.

The scanning head itself has no limitation for the marking speed. The process window for Ti-6Al-4V in SLM is comprised between 200 mm/s and 1600 mm/s [5,34,39,40,48,58,59]. We chose the value of 600 mm/s as a good compromise between build quality and acquisition frame rate of the X-ray detector.

Operando X-ray diffraction

The X-ray diffraction experiments have been performed at the MicroXAS beam line, located at the Swiss Light Source. The experiments were performed at an X-ray energy of 12 keV. In a first series of experiments the X-ray beam was focused down to $80 \times 36\ \mu m^2$ (full-width at half-maximum) with Kirkpatrick-Baez mirrors, resulting in a projected illuminated area of $80 \times 140\ \mu m^2$. For a second series, the beam had a projected illuminated area of $30 \times 35\ \mu m^2$. It should be noted that the tails of the X-ray beam extend to about twice these areas.

The diffracted beam is recorded by an in-house developed EIGER detector [60], which is an ultrafast single photon counting hybrid detector with small pixel size ($75 \times 75\ \mu m^2$), an active area of approximately $8 \times 4\ cm^2$ and contains 500,000 pixels. The detector is placed at 80 mm behind the sample and covers an angular range of $22° < 2\theta < 42°$. The detector was operated in 4 bit mode at a frame rate of 20 kHz with single frame exposure time of 45 μs. The lower energy threshold was set to 8 keV. Synchronization between the detector and laser operation was achieved over a hardware trigger.

The setup is calibrated with standard Al_2O_3 powder yielding the sample-to-detector distance, beam centre and detector tilt. The 2D images are reduced to conventional 1D diffraction patterns by azimuthal integration using the Bubble software package [61]. Single peak profile analysis was performed by in-house written Matlab routines. A measure for diffuse scattering was obtained by integrating the intensity between the (01.0) and (00.2) diffraction peaks.

Simulations

Finite element simulations were performed using the FE solver Abaqus [62] in transient heat transfer mode with hexahedral mesh. The results were used to illustrate this paper by plotting the computed node temperature at different time values.

The DFLUX subroutine was used to represent the laser scanning, which was modelled by a moving volumetric heat flux according to the modified Goldak's semi-ellipsoid model used by Zhang et al. [52]:

$$Q(x,y,z,t) = [2AP/(abc\pi\sqrt{\pi})]\exp[-((x+vt)^2/a + y^2/b + z^2/c)]$$

with A the absorptivity of the material, P the laser power in Watt; a, b and c the ellipsoid semi-axis, and v the scanning speed. Here $a = e.r$, $b = r/e$ and $c = d$ with e the melt pool eccentricity, r the laser radius and d the laser penetration depth. Details on this subroutines can be found in the software's user manual [63].

The material properties used are listed in Table T1 and T2 in Supplementary Data. The thermal conductivity of the powder was calculated using the equation of Sih and Barlow [64]. The density was approximated with the FCC packing coefficient [65]. The radiation and convection cooling was taken into account using the coefficient in Table T3 in Supplementary Data.

The powder bed was modelled as a whole volume occupying the first 30 μm of the volume thickness, and the rest was considered as bulk Ti-6Al-4V. These simulations do not incorporate all necessary physics to mimic the experiment, but where just done as a time-effective parametric study to illustrate the temperature distribution in the powder bed [65].

Declaration of Competing Interest

The authors declare that they have no known competing financial interests or personal relationships that could have appeared to influence the work reported in this paper.

Acknowledgements

This work was supported by (1) the PREcision Additive Manufacturing of Precious metals Alloys (PREAMPA) project, funded by the ETH board and the Swiss watch and precious metals industry; (2) the Additive Manufacturing and Metallic Microstructures (AM3) project, funded by the Competence Center for Materials Science and Technology (CCMX) and the Swiss watch and precious metals industry.

The support of Ulrich Frommherz (Engineering and Coordination, PSI), Beat Meyer and Mario Birri (MicroXAS beamline, SLS, PSI) is highly appreciated.

Appendix A. Supplementary data

Supplementary data to this article can be found online at https://doi.org/10.1016/j.mattod.2019.10.001.

References

[1] J. Yang et al., Mater. Des. 108 (2016) 308–318, https://doi.org/10.1016/j.matdes.2016.06.117.
[2] D.K. Do, P. Li, Virtual Phys. Prototyping 11 (2016) 41–47, https://doi.org/10.1080/17452759.2016.1142215.
[3] S. Liu, Y.C. Shin, Mater. Des. 164 (2019), https://doi.org/10.1016/j.matdes.2018.107552 107552.
[4] L. Liu et al., Mater. Today 21 (2018) 354–361, https://doi.org/10.1016/j.mattod.2017.11.004.
[5] J.J. Lewandowski, M. Seifi, Annu. Rev. Mater. Res. 46 (2016) 151–186, https://doi.org/10.1146/annurev-matsci-070115-032024.
[6] L. Tan Phuc, M. Seita, Mater. Des. 164 (2019), https://doi.org/10.1016/j.matdes.2018.107562 107562.
[7] M. Markl, C. Körner, Annu. Rev. Mater. Res. 46 (2016) 93–123, https://doi.org/10.1146/annurev-matsci-070115-032158.
[8] P. Stavropoulos, P. Foteinopoulos, Manuf. Rev. 5 (2018) 2, https://doi.org/10.1051/mfreview/2017014.
[9] S.A. Khairallah et al., Acta Mater. 108 (2016) 36–45, https://doi.org/10.1016/j.actamat.2016.02.014.
[10] P. Bajaj et al., Addit. Manuf. 27 (2019) 246–258, https://doi.org/10.1016/j.addma.2018.12.003.
[11] A.V. Gusarov et al., J. Heat Transfer 131 (2009), https://doi.org/10.1115/1.3109245 072101.
[12] L.-X. Lu, N. Sridhar, Y.-W. Zhang, Acta Mater. 144 (2018) 801–809, https://doi.org/10.1016/j.actamat.2017.11.033.
[13] W. Yan et al., Front. Mech. Eng. 13 (2018) 482–492, https://doi.org/10.1007/s11465-018-0505-y.
[14] P. Tan et al., Mater. Des. 168 (2019), https://doi.org/10.1016/j.matdes.2019.107642 107642.
[15] L. Wang et al., Int. J. Adv. Manuf. Technol. 97 (2018) 3535–3546, https://doi.org/10.1007/s00170-018-2207-3.
[16] Y. Zhang et al., Comput. Methods Appl. Mech. Eng. 331 (2018) 514–535, https://doi.org/10.1016/j.cma.2017.12.003.
[17] Z. Luo, Y. Zhao, Addit. Manuf. 21 (2018) 318–332, https://doi.org/10.1016/j.addma.2018.03.022.
[18] C. Luo et al., J. Mater. Process. Technol. 261 (2018) 74–85, https://doi.org/10.1016/j.jmatprotec.2018.06.001.
[19] Y. Du et al., Results Phys. 12 (2019) 52–60, https://doi.org/10.1016/j.rinp.2018.11.031.
[20] M. Chiumenti et al., Addit. Manuf. 18 (2017) 171–185, https://doi.org/10.1016/j.addma.2017.09.002.
[21] J. Ning et al., Materials 12 (2019) 808, https://doi.org/10.3390/ma12050808.
[22] T. Mukherjee et al., Comput. Mater. Sci. 150 (2018) 369–380, https://doi.org/10.1016/j.commatsci.2018.04.027.
[23] L. Scime, J. Beuth, Addit. Manuf. 25 (2019) 151–165, https://doi.org/10.1016/j.addma.2018.11.010.
[24] P.A. Hooper, Addit. Manuf. 22 (2018) 548–559, https://doi.org/10.1016/j.addma.2018.05.032.
[25] F. Wirth, S. Arpagaus, K. Wegener, Addit. Manuf. 21 (2018) 369–382, https://doi.org/10.1016/j.addma.2018.03.025.
[26] J. Trapp et al., Appl. Mater. Today 9 (2017) 341–349, https://doi.org/10.1016/j.apmt.2017.08.006.
[27] C. Kenel et al., JOM 68 (2016) 978–984, https://doi.org/10.1007/s11837-015-1774-0.
[28] C. Kenel et al., Sci. Rep. 7 (2017), https://doi.org/10.1038/s41598-017-16760-0.
[29] N.P. Calta et al., Rev. Sci. Instrum. 89 (2018), https://doi.org/10.1063/1.5017236 055101.
[30] C.L.A. Leung et al., Nat. Commun. 9 (2018), https://doi.org/10.1038/s41467-018-03734-7.
[31] C. Zhao et al., Sci. Rep. 7 (2017), https://doi.org/10.1038/s41598-017-03761-2.
[32] R. Boyer, G. Welsch, E.W. Collings (Eds.), Materials Properties Handbook: Titanium Alloys, 4. Printing, ASM International, Materials Park, Ohio, 2007.
[33] S.Y. Choy et al., Addit. Manuf. 16 (2017) 213–224, https://doi.org/10.1016/j.addma.2017.06.012.
[34] E. Onal et al., Metals 8 (2018) 200, https://doi.org/10.3390/met8040200.
[35] J. Dzugan et al., Mater. Charact. 143 (2018) 94–109, https://doi.org/10.1016/j.matchar.2018.04.003.
[36] C. de Formanoir et al., Mater. Sci. Eng., A 652 (2016) 105–119, https://doi.org/10.1016/j.msea.2015.11.052.
[37] P. Barriobero-Vila et al., Materials 10 (2017) 268, https://doi.org/10.3390/ma10030268.
[38] J. Haubrich et al., Acta Mater. 167 (2019) 136–148, https://doi.org/10.1016/j.actamat.2019.01.039.
[39] H. Gong et al., Addit. Manuf. 1–4 (2014) 87–98, https://doi.org/10.1016/j.addma.2014.08.002.
[40] C. Han et al., J. Mech. Behav. Biomed. Mater. 80 (2018) 119–127, https://doi.org/10.1016/j.jmbbm.2018.01.013.
[41] S. Yuan, C.K. Chua, K. Zhou, Adv. Mater. Technol. 4 (2019) 1800419, https://doi.org/10.1002/admt.201800419.
[42] T. Vilaro, C. Colin, J.D. Bartout, Metall. Mat. Trans. A 42 (2011) 3190–3199, https://doi.org/10.1007/s11661-011-0731-y.
[43] T.G. Spears, S.A. Gold, Integr. Mater. Manuf. Innov. 5 (2016) 16–40, https://doi.org/10.1186/s40192-016-0045-4.
[44] Y.S. Touloukian et al., Thermal Expansion, Springer US, Boston, MA, 1975. doi:10.1007/978-1-4757-1622-1.
[45] A. Zafari, M.R. Barati, K. Xia, Mater. Sci. Eng., A 744 (2019) 445–455, https://doi.org/10.1016/j.msea.2018.12.047.
[46] J.W. Elmer et al., J. Appl. Phys. 95 (2004) 8327–8339, https://doi.org/10.1063/1.1737476.
[47] A.V. Gusarov et al., Int. J. Heat Mass Transf. 46 (2003) 1103–1109, https://doi.org/10.1016/S0017-9310(02)00370-8.
[48] P. Kumar, O. Prakash, U. Ramamurty, Acta Mater. 154 (2018) 246–260, https://doi.org/10.1016/j.actamat.2018.05.044.
[49] M. Simonelli, Y.Y. Tse, C. Tuck, Metall. Mat. Trans. A 45 (2014) 2863–2872, https://doi.org/10.1007/s11661-014-2218-0.
[50] H. Ali, H. Ghadbeigi, K. Mumtaz, Mater. Sci. Eng., A 712 (2018) 175–187, https://doi.org/10.1016/j.msea.2017.11.103.
[51] J. Robinson et al., Addit. Manuf. 23 (2018) 13–24, https://doi.org/10.1016/j.addma.2018.07.001.
[52] Q. Zhang et al., Mater. Des. 166 (2019), https://doi.org/10.1016/j.matdes.2019.107618 107618.
[53] J.H. Martin et al., Nature 549 (2017) 365–369, https://doi.org/10.1038/nature23894.
[54] J. Zhang et al., J. Mater. Sci. Technol. 35 (2019) 270–284, https://doi.org/10.1016/j.jmst.2018.09.004.
[55] C. Genzel et al., J. Strain Anal. Eng. Des. 46 (2011) 615–625, https://doi.org/10.1177/0309324711403824.
[56] A.A. Coelho, J. Appl. Cryst. 51 (2018) 210–218, https://doi.org/10.1107/S1600576718000183.
[57] C. Cayron, J. Appl. Cryst. 40 (2007) 1183–1188, https://doi.org/10.1107/S0021889807048777.
[58] S.L. Campanelli et al., Materials (Basel) 7 (2014) 4803–4822, https://doi.org/10.3390/ma7064803.
[59] D. Agius, K. Kourousis, C. Wallbrink, Metals 8 (2018) 75, https://doi.org/10.3390/met8010075.
[60] G. Tinti et al. C03011-C3011, J. Instrum. 10 (2015), https://doi.org/10.1088/1748-0221/10/03/C03011.
[61] V. Dyadkin et al., J. Synchrotron Rad. 23 (2016) 825–829, https://doi.org/10.1107/S1600577516002411.
[62] Abaqus Unified FEA, (n.d.). https://www.3ds.com/products-services/simulia/products/abaqus/.
[63] Abaqus/CAE User's Guide, (n.d.). https://www.sharcnet.ca/Software/Abaqus/6.14.2/v6.14/books/usi/default.htm.
[64] S.S. Sih, J.W. Barlow, The Prediction of the Thermal Conductivity of Powders, in: 1995. doi:10.15781/T2ZW19C17.
[65] D.A. De Moraes, A. Czekanski, J. Manuf. Mater. Process. 2 (2018) 47, https://doi.org/10.3390/jmmp2030047.